J|A|C|S
ARTICLES

Published on Web 05/25/2010

Twisted Metal−Amino Acid Nanobelts: Chirality Transcription from Molecules to Frameworks

Chao Li,[†] Ke Deng,[†] Zhiyong Tang,*[,†] and Lei Jiang[‡]

Laboratory for Nanomaterials, National Center for Nanoscience and Technology, No. 11 Zhongguancun Beiyitiao, Beijing 100190, China, and Functional Interface Material Group, Key Laboratory of Organic Solids, Institute of Chemistry, Chinese Academy of Sciences, No. 2 Zhongguancun Beiyijie, Beijing 100190, China

Received April 4, 2010; E-mail: zytang@nanoctr.cn

Abstract: We have studied the self-assembly process of a typical biocoordination polymer, Ag(I)/cysteine (Cys), with different chiralities of the amino acid. Self-assembly of Ag(I)/L-Cys leads to production of pure right-handed helical nanobelts, whereas Ag(I)/D-Cys gives rise to the "mirror image", i.e., pure left-handed helical nanobelts. As a comparison, racemic Ag(I)/DL-Cys forms a totally different product, two-dimensional achiral nanosheets. Density functional theory simulation revealed that the molecular chirality of Cys is originally programmed in the specific lattice twisting, which further determines the chirality and dimensionality of the assembly products. This understanding will shed light on comprehending chirality transcription in metal−organic frameworks as well as designing chirality-regulated nanosuperstructures.

Introduction

Coordination polymers (CPs), in which small organic molecules are linked by metal ions through primary coordination interactions and further grow into advanced structures through multiple weak interactions such as hydrogen bonding and van der Waals forces, represent a novel type of functional nanomaterial and have attracted much scientific interest.[1,2] Recent studies highlight potential applications of nanoscale CPs in many fields,[3] such as energy,[4] catalysis,[5] sensing,[6] and biomedicine.[7]

Herein, we suggest using natural amino acids to replace conventional synthetic molecules as building blocks of CPs, to give so-called bio-CPs (BCPs). BCPs, consisting of amino acid units linked by metal ions through coordination interactions, are structurally analogous to peptide chains and considered to be a promising motif for "programmed" design of nanomaterials. Because of the unique properties and functionalities of amino acid molecules achieved from natural selection,[8] the design and fabrication of BCPs will help us to take advantage of the warehouse of natural ligands and expand the toolbox of nanofabrication.[9,10] For example, in contrast to many synthetic organic molecules, the primary structures of the 20 natural amino acids are chiral and exclusively in the L forms, which are selectively recognized and arranged into ribosomes and further assembled into proteins. The homochirality of the amino acid building blocks determines the nature of higher-order structures in the proteins [e.g., the right-handed α-helix (secondary structure) and the fold (tertiary structure)].[11] BCPs will provide an excellent platform for understanding both chirality transcription of amino acids to BCPs and the detailed self-assembly process from small biomolecules to macroscopic coordination frameworks, which is paramount not only for biomimetic fabrication of novel materials but also for understanding many biorelated processes.[12,13]

Guided by this principle, we constructed a series of coordination frameworks composed of the amino acid cysteine (Cys) and Ag(I) cation. Both circular dichroism (CD) and scanning electron microscopy (SEM) indicated that the morphological evolution in the homochiral Ag(I)/Cys system starts with the transformation of Ag(I)/Cys BCPs first to nanofibrils, subsequently to nonhelical nanobelts by hierarchical attachment, and finally to single-crystal helical nanobelts with homochirality.

[†] National Center for Nanoscience and Technology.
[‡] Institute of Chemistry.

(1) Batten, S. R.; Robson, R. *Angew. Chem., Int. Ed.* **1998**, *37*, 1460–1494.
(2) Gianneschi, N. C.; Masar, M. S.; Mirkin, C. A. *Acc. Chem. Res.* **2005**, *38*, 825–837.
(3) Long, J. R.; Yaghi, O. M. *Chem. Soc. Rev.* **2009**, *38*, 1213–1214.
(4) (a) Czaja, A. U.; Trukhan, N.; Müller, U. *Chem. Soc. Rev.* **2009**, *38*, 1284–1293. (b) Murray, L. J.; Dincă, M.; Long, J. R. *Chem. Soc. Rev.* **2009**, *38*, 1294–1314.
(5) Ma, L. Q.; Abney, C.; Lin, W. B. *Chem. Soc. Rev.* **2009**, *38*, 1248–1256.
(6) Allendorf, M. D.; Bauer, C. A.; Bhakta, R. K.; Houk, R. J. T. *Chem. Soc. Rev.* **2009**, *38*, 1330–1352.
(7) (a) Kim, J. S.; Rieter, W. J.; Taylor, K. M. L.; An, H. Y.; Lin, W. L.; Lin, W. B. *J. Am. Chem. Soc.* **2007**, *129*, 8962–8963. (b) Rieter, W. J.; Pott, K. M.; Taylor, K. M. L.; Lin, W. B. *J. Am. Chem. Soc.* **2008**, *130*, 11584–11585.
(8) Yamauchi, O.; Odani, A.; Takani, M. *J. Chem. Soc., Dalton Trans.* **2002**, 3411–3421.
(9) Mantion, A.; Massüger, L.; Rabu, P.; Palivan, C.; McCusker, L. B.; Taubert, A. *J. Am. Chem. Soc.* **2008**, *130*, 2517–2526.
(10) Imaz, I.; Martínez, M. R.; Saletra, W. J.; Amabilino, D. B.; Maspoch, D. *J. Am. Chem. Soc.* **2009**, *131*, 18222–18223.
(11) Elemans, J. A. A. W.; Rowan, A. E.; Nolte, R. J. M. *J. Mater. Chem.* **2003**, *13*, 2661–2670.
(12) (a) Lee, C. C.; Grenier, C.; Meijer, E. W.; Schenning, A. P. H. J. *Chem. Soc. Rev.* **2009**, *38*, 671–683. (b) Smith, D. K. *Chem. Soc. Rev.* **2009**, *38*, 684–694. (c) Tanaka, K.; Clever, G. H.; Takezawa, Y.; Yamada, Y.; Kaul, C.; Shionoya, M.; Carell, T. *Nat. Nanotechnol.* **2006**, *1*, 190–194. (d) Yoon, S. M.; Hwang, I. C.; Shin, N.; Ahn, D.; Lee, S. J.; Lee, J. Y.; Choi, H. C. *Langmuir* **2007**, *23*, 11875–11882. (e) Chen, H. B.; Zhou, Y.; Yin, J.; Yan, J.; Ma, Y. G.; Wang, L.; Cao, Y.; Wang, J.; Pei, J. *Langmuir* **2009**, *25*, 5459–5462.
(13) Mann, S. *Angew. Chem., Int. Ed.* **2008**, *47*, 5306–5320.

10.1021/ja102827f

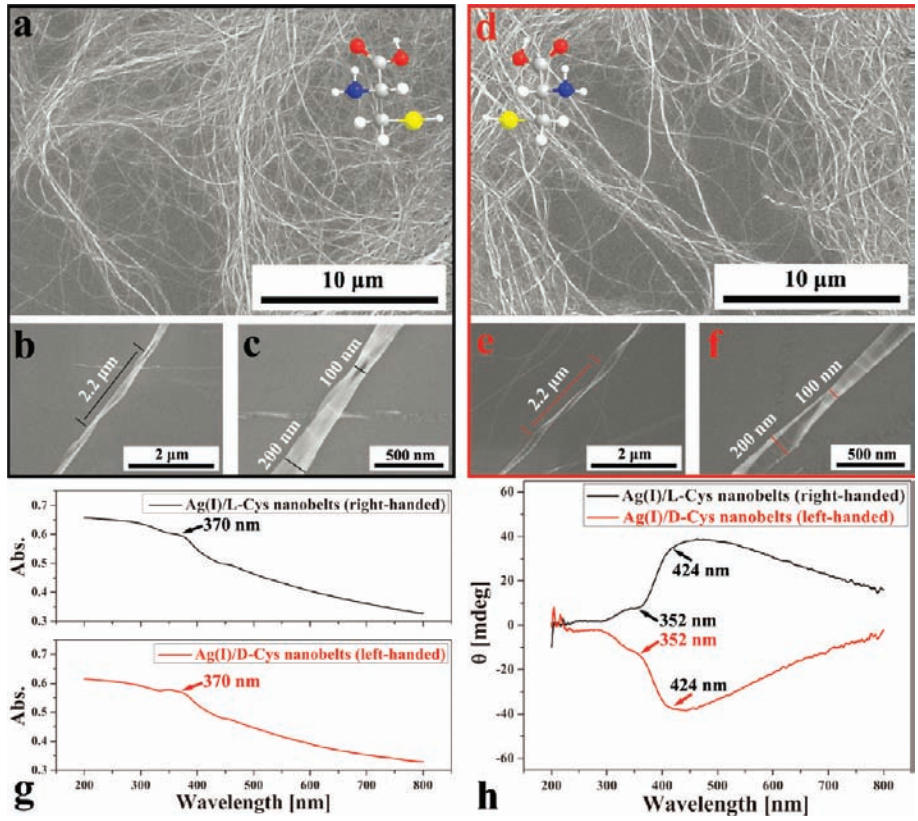

Figure 1. Self-assembled Ag(I)/Cys helical nanobelts with homochirality. (a) Large-area and (b, c) high-resolution SEM images of Ag(I)/L-Cys nanobelts, in which the helix is right-handed. (d) Large-area and (e, f) high-resolution SEM images of Ag(I)/D-Cys nanobelts, in which the helix is left-handed. The helical belts are tens of micrometers long and partially closed, and the width of the helix varies from 100 nm (the narrowest part) to 200 nm (the widest part). The helical pitch is ∼2 μm. (g) UV−vis spectra of the two types of Ag(I)/Cys helical nanobelts. (h) Corresponding CD spectra. The insets in (a) and (d) illustrate the molecular structures of L-Cys and D-Cys: C, gray; H, white; O, red; N, dark-blue; S, yellow.

Unexpectedly, two-dimensional (2D) achiral nanosheets were formed from the racemic Ag(I)/DL-Cys system. Crystal structure analysis and computational simulation revealed that the chirality and dimensionality of the final assemblies are originally "programmed" by the ligand's chirality and the metal−ligand interactions.

Results and Discussion

Ag(I)/Cys Homochiral Helical Nanobelts: Morphology and Chirality. The self-assembly processes and products of CPs and BCPs are susceptible to the reaction conditions, such as precursor concentration and molar ratio, pH of the medium, and reaction temperature. Generally, fast assembly leads to the formation of amorphous products,[14] whereas relatively slow assembly is essential for preparing crystalline metal−organic frameworks (MOFs).[15] Such is the case for the Ag(I)/Cys system. The reaction conditions were rationalized as follows in order to obtain Ag(I)/Cys BCPs with well-defined structure: 0.15 mM $AgClO_4$ and 0.25 mM Cys were mixed in aqueous solution at a pH of ∼10.45 and then heated to 37 °C (human body temperature) (see Part S1 in the Supporting Information). In addition, the above Ag(I)/Cys self-assembly could also occur at least at 23 °C (room temperature) (see Figure S1 in the Supporting Information), which makes a relatively broad temperature window for the potential applications.

After 6−8 days, the self-assembled products of Ag(I)/L-Cys were observed to be exclusively right-handed helical nanobelts, and neither nanobelts with opposite handedness nor materials with other shapes could be discerned from the SEM images (Figure 1a). Thus, it is reasonably concluded that the Ag(I)/L-Cys nanobelts had right-handed homochirality. The nanobelts were tens of micrometers long with a typical helical pitch of ∼2 μm, while the width of the helix varied from 100 to 200 nm for the twisted and stretched morphologies, respectively (Figure 1b,c). On the contrary, Ag(I)/D-Cys was found to be the "mirror image", pure left-handed helical nanobelts with almost the same size parameters (Figure 1d−f). Interestingly, similar chirality selection also happens in nature, where almost all biological amino acids (except for glycine) have L-type chirality while the α-helices in proteins are exclusively right-handed. The "mirror image" relationship of the two types of Ag(I)/Cys BCP helix was found not only in their morphologies but also in their optical properties. Although the two helical belts had identical UV−vis absorption characteristics with a shoulder peak at ∼370 nm (Figure 1g), which should arise from the coupling low-energy ligand-to-metal charge-transfer bands in the extended coordination frameworks,[16] the bisignate Cotton effects centered at 352 and 424 nm in the CD spectra displayed opposite symmetries (Figure 1h).[17]

(14) Spokoyny, A. M.; Kim, D.; Sumrein, A.; Mirkin, C. A. *Chem. Soc. Rev.* **2009**, *38*, 1218–1227.
(15) Lin, W. B.; Rieter, W. J.; Taylor, K. M. L. *Angew. Chem., Int. Ed.* **2009**, *48*, 650–658.
(16) Fijolek, H. G.; Grohal, J. R.; Sample, J. L.; Natan, M. J. *Inorg. Chem.* **1997**, *36*, 622–628.
(17) Horada, N.; Nakanishi, K. *Circular Dichroic Spectroscopy: Exciton Coupling in Organic Stereochemistry*; University Science Books: Mill Valley, CA, 1983.

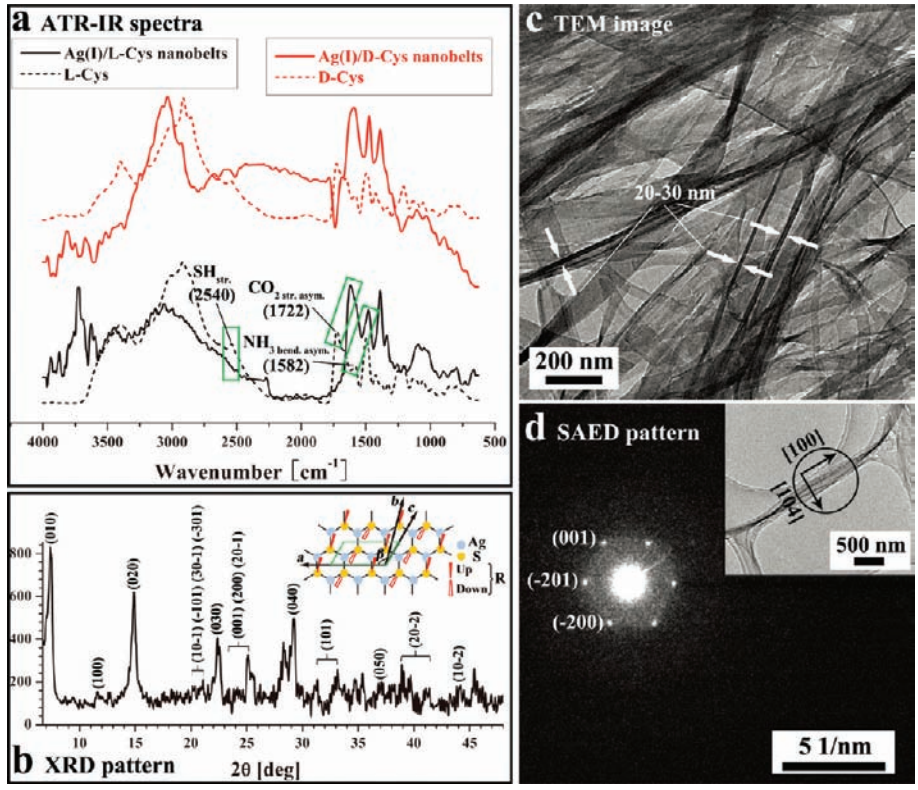

Figure 2. Composition and crystal structure analysis of the Ag(I)/Cys helical nanobelts. (a) ATR-IR spectra of the helical belts (solid lines) and corresponding Cys (dashed lines). The significant peaks and corresponding groups are labeled. In the helical belts, the mercapto (−SH) group disappears and the carboxyl (−COOH) and amino ($-NH_2$) groups are obviously red-shifted, as shown by the comparisons in the three inset green frames. (b) XRD pattern. This pattern is similar to that adopted by Ag−alkylthiolate coordination polymers. The inset shows the layered structure, which contains parallel quasi-hexagonal slabs of connected Ag (light-blue) and S (yellow) atoms, with the R groups (red) on S inclined perpendicular (or nearly perpendicular) to each slab and extending from both sides of it. The theoretical 2D unit cell is drawn in green lines. Artificial symmetry was introduced by the theoretical dimensions $a = 8.70$ Å, $c = 4.35$ Å, and $\beta = 120°$. The interlayer distance b is in proportion to the length of the R group; here $b = 12.01$ Å. The d spacings of the interlayer (axial) reflections (0k0) are listed in Table S2 in the Supporting Information, and the ones of the intralayer (nonaxial) reflections (h0l) are listed in Table S3. (c) TEM image. The typical thickness of the belts is 20−30 nm. (d) SAED pattern. The black circle in the inset shows the corresponding selected area for electron diffraction. The SAED pattern reveals a single-crystal structure with quasi-hexagonal symmetry. The incident direction of electron beam was along [010]. The helix's length and width directions are along [100] and [104], respectively. The d spacings of the three labeled crystal planes are 4.12−4.40 Å.

Ag(I)/Cys Homochiral Helical Nanobelts: Composition and Structure. The structures of the Ag(I)/Cys BCPs were investigated in detail (Figure 2). First, energy-dispersive X-ray (EDX) analysis showed that the Ag/S and Ag/O atomic ratios in these helical belts are about 1:1 and 1:2, respectively (Figure S2 and Table S1 in the Supporting Information), which can be initially attributed to the Ag thiolate with molecular formula $\{AgSR\}_n$ [where R is $-CH_2CH(NH_2)COOH$]. Second, the attenuated total reflection infrared (ATR-IR) spectra indicated that the SH stretching peak at 2540 cm^{-1} for Cys totally disappears in the Ag(I)/Cys helical belts (Figure 2a), confirming that $\{AgSR\}_n$ BCPs are formed through strong Ag−S coordination bonds. Meanwhile, the obvious red shifts of both the CO_2 asymmetric stretching at 1722 cm^{-1} and the NH_2 asymmetric bending at 1582 cm^{-1} for Cys denote associated interactions between $\{AgSR\}_n$ in the 3D lattice (further discussed below in DFT Simulation of Chirality Transcription).[18] Third, the crystal structure of the Ag(I)/Cys helical belts obtained by powder X-ray diffraction (XRD) can be assigned to $\{AgSR\}_n$ layered structures in which R substituents extend perpendicularly to both sides of a central slab of Ag and S atoms (Figure 2b and inset). As a result of preferential orientation, the reflections (0k0) from the axial direction normal to the layers are distinct and appear in the XRD pattern as a series of strong, equidistant peaks with k up to 5 (Figure 2b). The average thickness of one layer calculated from the (0k0) reflections is ∼12.01 Å (Table S2 in the Supporting Information), which suggests the interconnection of the carboxyl groups between the adjacent Ag−S slabs. Moreover, the rather weak reflections in the XRD pattern are mostly from (h0l) and depict the periodic structure within the Ag−S slab (Figure 2b and Table S3 in the Supporting Information). It should be noted that such intralayer structure is a common feature of $\{AgSR\}_n$ crystalline compounds, and similar diffraction patterns have been found for Ag−alkylthiolate coordination polymers.[19] Finally, both transmission electron microscopy (TEM) and selected-area electron diffraction (SAED) were used to check the crystalline nature of the Ag(I)/Cys helical belts. The belts are very thin (20−30 nm), and twists can be clearly discerned in the TEM image (Figure 2c). The SAED pattern further revealed that such helical belts have a single-crystal structure with quasi-hexagonal symmetry (Figure 2d). It should be pointed out that high-resolution TEM (HRTEM) images of the helices could not be obtained in the current study because the Ag(I)/Cys helical belts were very easily destroyed

(18) Hooper, R. J.; Lane, T. J.; Walter, J. L. *Inorg. Chem.* **1964**, *3*, 1568–1573.

(19) Dance, I. G.; Fisher, K. J.; Banda, R. M. H.; Scudder, M. L. *Inorg. Chem.* **1991**, *30*, 183–187.

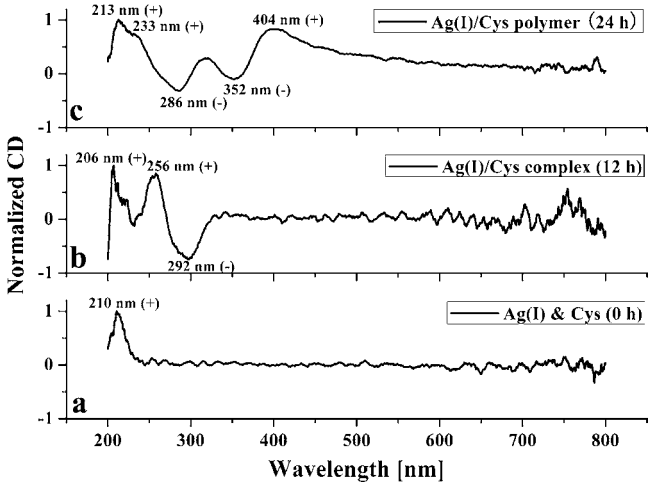

Figure 3. Monitoring of the Ag(I)/Cys BCP formation process by CD spectroscopy. (a) CD spectrum of the beginning mother solution composed of Ag(I) and Cys with a pH of ∼10.45. (b) CD spectrum of the Ag(I)/Cys complex formed after 12 h of reaction of the mother solution at 37 °C. (c) CD spectrum of the Ag(I)/Cys polymer formed after 24 h of reaction.

under electron beam irradiation (Figure S4 in the Supporting Information). Nevertheless, armed with the above characterizations, we assumed that Ag(I) and Cys form 2D slabs through Ag−S coordination interactions with length and width along [100] and [104], respectively, and that along [010] the slabs are interconnected into 3D frameworks via hydrogen bonding between Cys carboxyl groups. This is somewhat reminiscent of the layered structures widely observed in chiral self-assemblies of polypeptides.[20]

Ag(I)/Cys Homochiral Helical Nanobelts: Intermediate Self-Assembly States and Growth Mode. How do the Ag(I) and Cys precursors spontaneously evolve into the helical nanobelts with homochirality? The intermediate states of the corresponding self-assembly processes were explored using both spectroscopy and microscopy techniques. At the very beginning of the growth process, only one chiral peak at 210 nm, contributed by Cys molecules, was observed in the CD spectrum (Figure 3a and Figure S5a−c in the Supporting Information). After 12 h of reaction, one pair of peaks centered at 256 and 292 nm appeared; this is a typical bisignate Cotton effect corresponding to the UV−vis shoulder peak around 280 nm (Figure S5d in the Supporting Information) (Figure 3b). As in the previous study, such chirality signals can be assigned to the formation of simple Ag(I)/Cys complexes in the mother solution.[21] After another 12 h interval, a new bisignate Cotton effect centered at 352 and 404 nm was observed, corresponding to the UV−vis shoulder peak at ∼362 nm (Figure 3c and Figure S5e in the Supporting Information). In analogy to the discussion of Figure 1g,h, this denotes the further growth of the Ag(I)/Cys complexes into BCPs with extended coordination frameworks.

In the subsequent self-assembly process, although no new chiral peaks appeared during further CD monitoring, the shape of the homochiral Ag(I)/Cys BCPs was found to have a tremendous change (Figure 4). The 1-day product took the form of nanofibrils (20−40 nm wide and ∼1 μm long) (Figure 4a), which further evolved into longer nonhelical belts with widths of ∼100 nm and lengths of several micrometers after another day's growth (Figure 4b). The nonhelical belts continued assembling and merging with each other through lateral attachment, developing into the hierarchical helices with a specific twist direction (Figure 4c). The partially helical and partially nonhelical belts were just the intermediates in the formation of the final helix products. Once the helices formed, the twisted parts no longer merged with each other, while the other nonhelical belts or parts kept on assembling until they twisted (Figure 4d). When the growth time was long enough, the final products were all homochiral helical nanobelts with a helix width varying from 100 to 200 nm and lengths of tens of micrometers (Figure 4e).

From the above study of the intermediate states, three distinct assembly features are concluded: (I) The process of forming the Ag(I)/Cys BCP nanostructures is hierarchical. The assembly starts from the formation of Ag(I)/Cys complexes, which then develop into BCPs. The BCPs preliminarily exist as short nanofibrils and gradually grow into nanohelices of specific chirality with increasing length and width. (II) The assembly rate in the length direction is faster than that in the width direction, and lateral attachment is one of the important modes for width growth.[22] (III) The specific twisting of the belts is width-determined, and the critical width for helix formation is ∼200 nm (it should be noted that when the belts evolve into helices, the width changes from 200 nm to 100−200 nm because of the partially closed twisting.). In order to confirm the dependence of width on helix formation, disassembly of the helical nanobelts was performed by irradiation with UV light (365 nm/54 mW cm^{-2}/30 min).[23] The cleavage preferentially occurred along the belt's perimeter, and the helix structure disappeared in the narrowed parts (Figure S6 in the Supporting Information).

DFT Simulation of Chirality Transcription in Ag(I)/Cys Homochiral Frameworks. Why can the interaction between Ag(I) and Cys molecules with different chiralities give rise to the production of helical nanobelts with different handedness? Here, density functional theory (DFT) simulation was used to understand the chirality transcription and dimension determination of the Ag(I)/Cys BCPs. All of the Ag(I)/Cys lattices in the simulations were constructed in a right-handed Cartesian coordinate system based on the experimental crystal structure data. For each initial lattice [Ag(I)/L-Cys, Ag(I)/D-Cys, and Ag(I)/DL-Cys], there was no structural chirality. Next, the initial lattices were optimized by DFT calculation. The relationship between Cartesian coordinate axes and crystal axes was defined as follows: Z is a; Y is $-b$; for Ag(I)/L-Cys and Ag(I)/DL-Cys lattices, X is [104]; for the Ag(I)/D-Cys lattice, X is [$\bar{1}0\bar{4}$].

In order to trace the specific twisting of each lattice, we selected four groups of S atoms with initial translation equivalence, each group containing two S atoms. After energy optimization, it was found that the introduction of ligand homochirality into the 3D Ag(I)/Cys lattice breaks the initial translation equivalence and results in specific twist accumulation. The coordinates of the eight S atoms for each homochiral lattice are listed in Table S4 in the Supporting Information. As shown in Figure 5, the numbering mode "Xn-m" is utilized to discriminate the eight lattice points with respect to each other

(20) (a) Branco, M. C.; Nettesheim, F.; Pochan, D. J.; Schneider, J. P.; Wagner, N. J. *Biomacromolecules* **2009**, *10*, 1374–1380. (b) Shao, H.; Nguyen, T.; Romano, N. C.; Modarelli, D. A.; Parquette, J. R. *J. Am. Chem. Soc.* **2009**, *131*, 16374–16376. (c) Cui, H. G.; Muraoka, T.; Cheetham, A. G.; Stupp, S. I. *Nano Lett.* **2009**, *9*, 945–951.
(21) Lock, H. E. H. *Met.-Based Drugs* **1999**, *6*, 201–209.
(22) Banfield, J. F.; Welch, S. A.; Zhang, H. Z.; Ebert, T. T.; Penn, R. L. *Science* **2000**, *289*, 751–754.
(23) Balzani, H.; Carassiti, V. *Photochemistry of Coordination Compounds*; Academic Press: London, 1970.

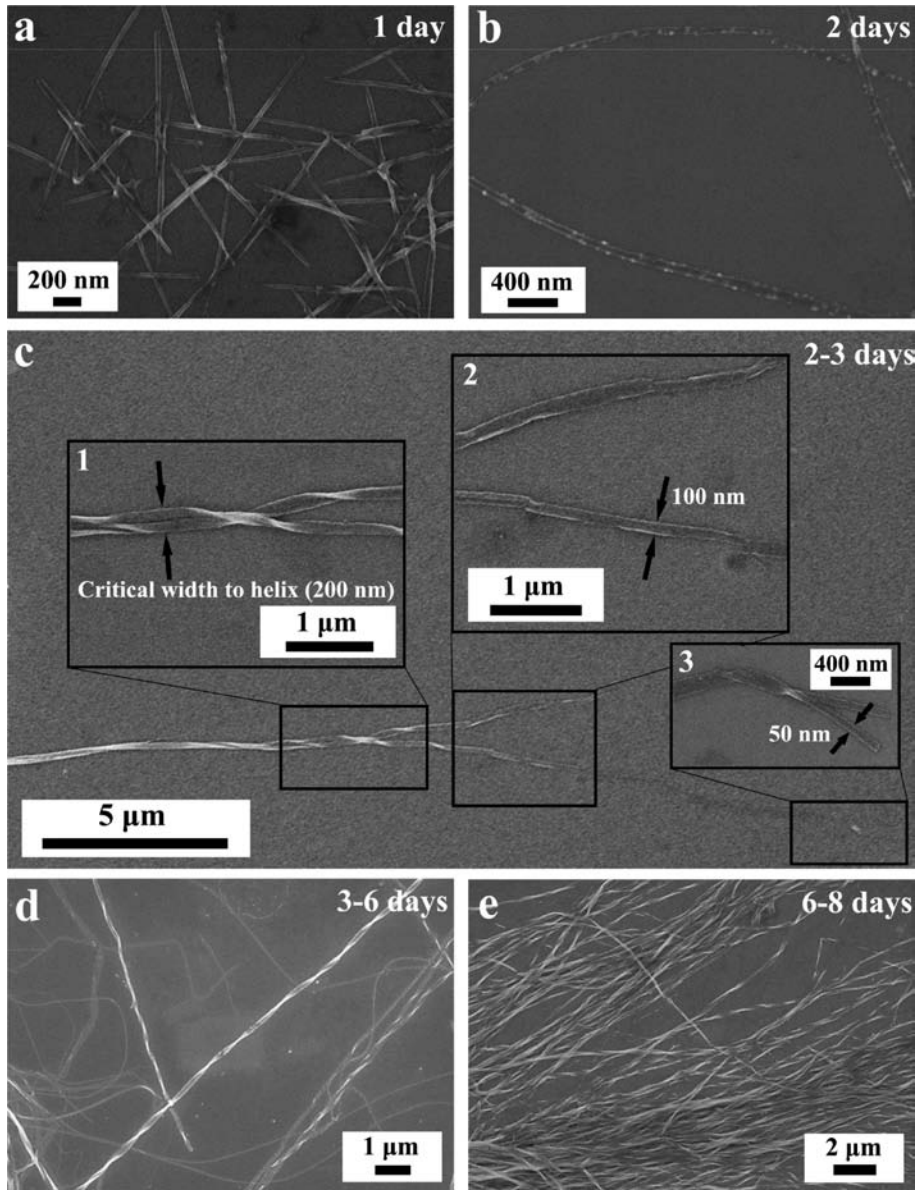

Figure 4. Morphological evolution of the homochiral Ag(I)/Cys BCPs monitored by SEM. (a) Nanofibrils formed after 1 day (20−40 nm wide, ∼1 μm long). (b) Nonhelical nanobelts formed after 2 days (∼100 nm wide, several micrometers long). (c) BCP nanobelt with both helical and nonhelical parts (2−3 days). Insets (1−3) show amplified parts of the partially helical and partially nonhelical belt: (1) transitional part connecting the generated helix and the constituent sub-belts; (2) the two constituent nonhelical belts (∼100 nm wide); (3) tip of one nonhelical belt further composed of two 50 nm wide sub-belts. (d) mixture of helical nanobelts with nonhelical nanobelts formed after 3−6 days. (e) homochiral helical nanobelts formed after 6−8 days, with a helix width varying from 100 to 200 nm and lengths of tens of micrometers.

because of the loss of initial translation equivalence. In this notation, X = N or F, which stand for "near end" or "far end", respectively; n = 1 or 2, which represent "former" or "latter", respectively; and m = 1 or 2, which represent "up" or "down", respectively. There are three important criteria in Figure 5c for distinguishing the chirality in the Ag(I)/L-Cys lattice: (I) In the right geometric frame of Figure 5c, the distance between N2-1 and N1-2 in the *XY* plane ($\Delta N_{X\text{-}Y}$) is shorter than that between F2-1 and F1-2 ($\Delta F_{X\text{-}Y}$) (12.781 vs 13.202 Å). This is consistent with the fact that for a helical nanobelt, the circumference of the inner layer ("near end") should be smaller than that of outer layer ("far end"). (II) Also in the right geometric frame of Figure 5c, the "up" plane constructed with bright-yellow points of F1-1, F2-1, N1-1, and N2-1 shows larger *X* values than the "down" plane constructed with brown points of F1-2, F2-2, N1-2, and N2-2. In combination with criterion (I), this shows that the outer layer undergoes an anticlockwise movement in the *XY* plane. (III) In the left geometric frame of Figure 5c, the "latter" plane constructed with the four points of F2-1, N2-1, F2-2, and N2-2 shows larger *Z* values than the "former" plane constructed with the points of F1-1, N1-1, F1-2, and N1-2. Armed with the above criteria, one can see that the twist direction of the Ag(I)/L-Cys lattice is anticlockwise (the right geometric frame of Figure 5c) and up (the left geometric frame of Figure 5c) when using the intersection point (O) of the two radial rays F1-2−N1-2 and F2-1−N2-1 as the middle axis. Thus, it can be concluded that there is right-handed twist accumulation in Ag(I)/L-Cys frameworks, leading to the formation of a right-handed helix as the final product. A similar analysis was done for the Ag(I)/D-Cys lattice (Figure 5f), and the helix of the corresponding product was found to be left-handed.

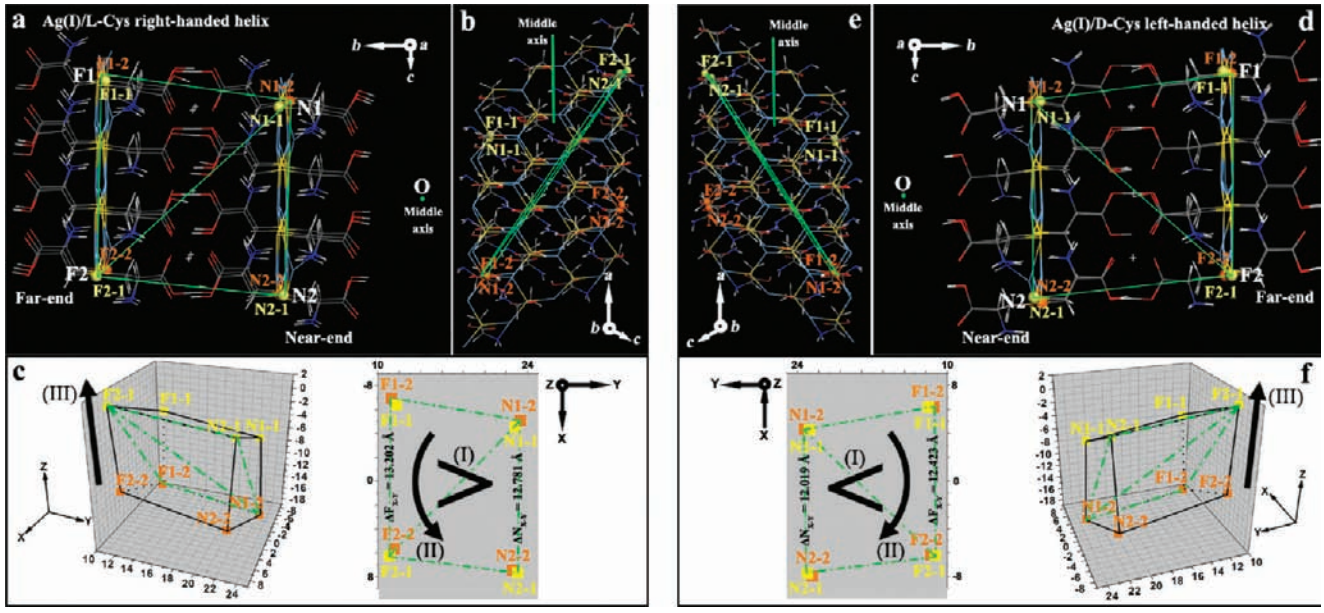

Figure 5. Illustration of the optimized simulation results for the homochiral Ag(I)/Cys lattices. (a) Top view (−*a* direction) of the optimized Ag(I)/L-Cys lattice segment. To discriminate along the *a* direction, the four S atoms in the "up" plane are labeled in bright-yellow and the four in the "down" plane in brown. The green tetragon used for following estimation was constructed with the four points F2-1, N2-1, N1-2, and F1-2. In it, F2-1−N1-2 represents the diagonal line linking the highest and lowest S atoms. For each homochiral lattice, the part that is close to the middle axis of the helix is defined as the "near end" (inner layer), while the part in the remote direction is the "far end" (outer layer). (b) Side view (−*b* direction) of the optimized Ag(I)/L-Cys lattice segment, showing that the eight S atoms are selected from a 3 × 3 Ag−S double slab. The green tetragon and diagonal line correspond to those in (a). (c) Geometric frames drawn from the eight Cartesian coordinates. (d−f) Same as (a−c) for the optimized Ag(I)/D-Cys lattice segment. C, gray; H, white; O, red; N, dark-blue; S, yellow; Ag, light-blue.

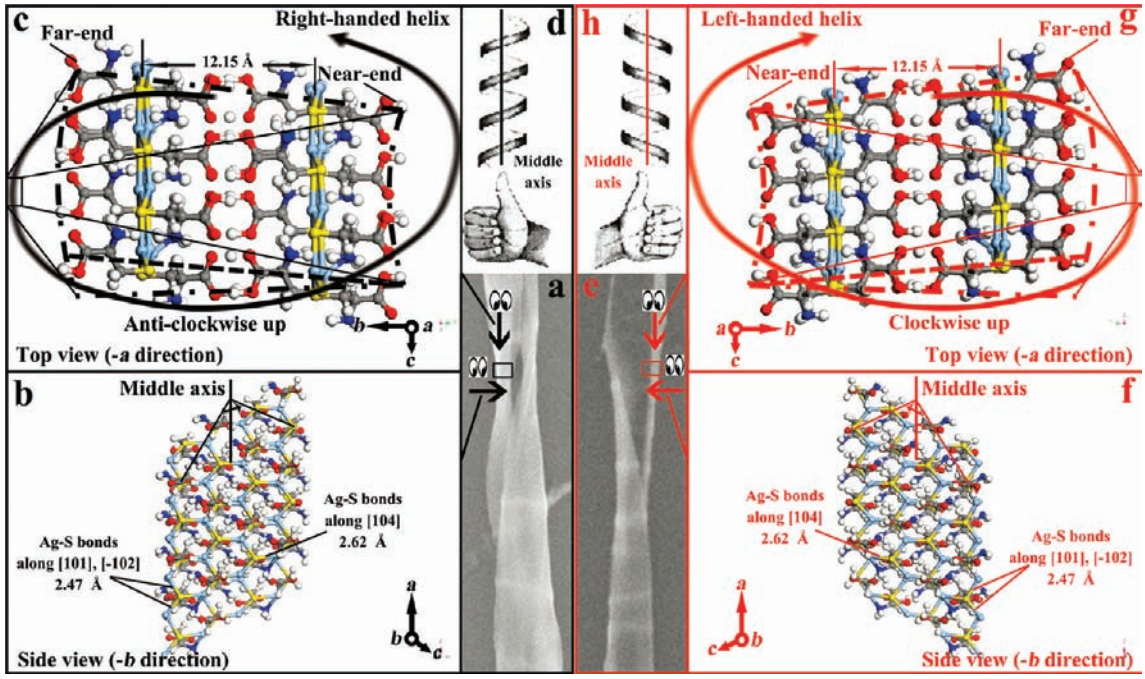

Figure 6. 3D crystal structures of (left) the right-handed Ag(I)/L-Cys helical belt and (right) the left-handed Ag(I)/D-Cys helical belt obtained by DFT simulation. (a) Local amplification of the right-handed helical belt. The rectangular frame shows the cut-out piece corresponding to the following optimized lattice segment in (b) and (c). For each lattice, the *a*, *b*, and *c* directions show the three crystal axes. (b) Side view (−*b* direction) of the lattice segment of the Ag(I)/L-Cys helical belt. The Ag−S bonds along [104] are longer and weaker than those along [101] and [$\bar{1}$02]. (c) Top view (−*a* direction) of the lattice segment of the Ag(I)/L-Cys helical belt. The anticlockwise upward spiral arrow denotes the right-handedness, and the rectangular frame shows the macroscale location of the lattice segment in the helix. The optimized interlayer distance is 12.15 Å. (d) Schematic illustration of a right-handed helix. The solid line shows the middle axis. The thumb points in the +*a* direction. The part that is close to the middle axis of the helix is defined as the "near end", and the part in the remote direction is the "far end". The dash-dot frame in the top-view picture is an amplified illustration showing the specific twist between the near end and the far end. The dashed line shows the near end's hypothetical translation border without twist. (e−h) Same as (a−d) for the left-handed Ag(I)/D-Cys helical belt. C, gray; H, white; O, red; N, dark-blue; S, yellow; Ag, light-blue.

The optimized 3D crystal structures of the homochiral Ag(I)/Cys helical nanobelts obtained from the above simulation are shown in Figure 6. The strong Ag−S interaction (47.11 kcal mol^{-1} on average) is responsible for the formation of the

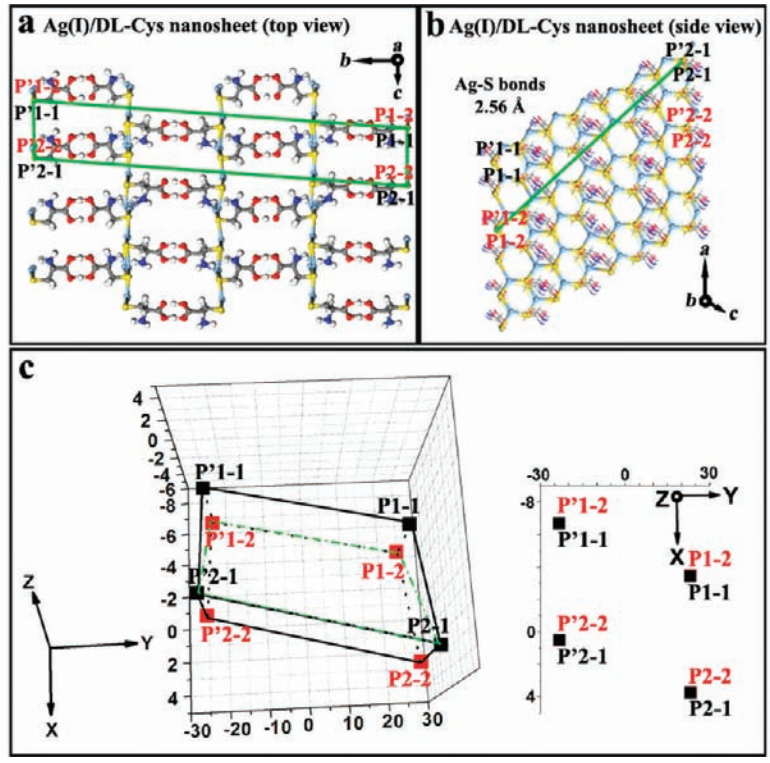

Figure 7. Illustration of the optimized results for the racemic Ag(I)/DL-Cys lattice. (a) Top view ($-a$ direction) of the optimized Ag(I)/DL-Cys lattice segment. (b) Side view ($-b$ direction) of the optimized Ag(I)/DL-Cys lattice segment. There is no intralayer asymmetry of the Ag−S bonds, and the average Ag−S bond length is close to the theoretical value (2.56 Å). (c) Geometric frames drawn from the eight Cartesian coordinates. The green tetragon P2-1−P'2-1−P'1-2−P1-2 was used for calculating the intermediate parameters. The calculated results show that the specific twist accumulation in homochiral systems disappears here. C, gray; H, white; O, red; N, dark-blue; S, yellow; Ag, light-blue.

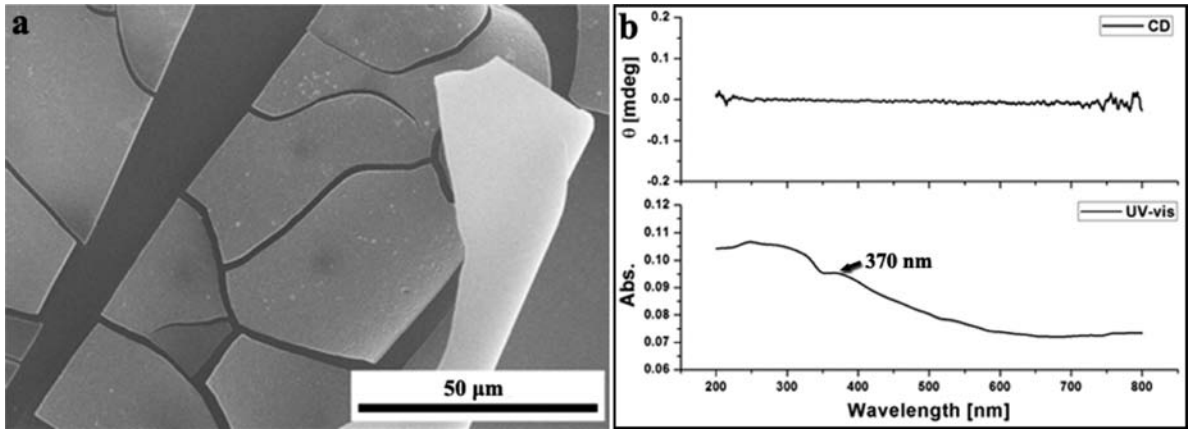

Figure 8. (a) SEM image of the racemic Ag(I)/DL-Cys nanosheets and (b) corresponding UV and CD spectra.

intralayer quasi-hexagonal Ag−S network. It is interesting that the introduction of homochiral Cys molecules results in the formation of asymmetric Ag−S bonds that discriminate between the intralayer directions (Figure 6b,f). The Ag−S bonds in [101] and [$\bar{1}$02] are shorter and stronger than those in [104]. This is the reason why the assembly rate in the length direction, [100], is faster than that in the width direction, [104]. In the thickness direction, [010], two layers are connected via strong O−H···O hydrogen bonds (29.60 kcal mol^{-1} on average) between the end carboxyl groups of the Cys molecules (Figure S7 in the Supporting Information). The optimized interlayer distance is 12.15 Å, which is in agreement with the experimental value of 12.01 Å from the XRD characterization (Table S2 in the Supporting Information). The energy comparison in different directions in the Ag(I)/Cys coordination frameworks is the basis for the final formation of belt morphology (length of over 10 μm, width of ~200 nm, thickness of 20−30 nm). More importantly, the introduction of homochiral Cys molecules gives rise to the specific twist accumulation in the Ag(I)/Cys coordination frameworks (Figure 6c,g). L-Cys leads to a right-handed helical lattice, and conversely, D-Cys results in a left-handed helical lattice. On the basis of calculations from our optimized models, the narrowest width and pitch of the helical belts are 75 nm and 2.3 μm, respectively; furthermore, the determined width of a nanobelt that can form a helix is 237 nm (see the detailed calculations in Part S3.3, Figure S8, and Table S5 in the Supporting Information). All of the simulation results are quite consistent with the experimental observations.

At last, another question arises naturally: what happens in the aqueous solution of racemic Ag(I)/DL-Cys? It is easy to expect the result to be a mixture of right-handed and left-handed helical belts or nonhelical belts. Unexpectedly, further simulation revealed that when the racemic Cys molecules are introduced into the Ag(I)/Cys frameworks, the asymmetry of the intralayer Ag−S bonds and the specific twist accumulation in the homochiral frameworks are both eliminated, so the positions of "near/far", "up/down", and "former/latter" among the eight selected S atoms cannot be discriminated (Figure 7 and Table S6 in the Supporting Information). The calculations were also based on the tetragon constructed with P2-1, P'2-1, P'1-2, and P1-2, and the definitions of the intermediate parameters are the same with the homochiral systems. The comparison of the calculated results clearly shows that the initial translation equivalence is greatly broken in the two homochiral lattices, whereas it is kept almost unchanged in the racemic lattice (Table S7 in the Supporting Information). In conclusion, for the racemic system, Ag(I) and Cys are linked together through strong Ag−S bonds into 2D networks without a difference in intralayer directions, and there is also no specific twist accumulation. The "flat" Ag−S slabs are further connected with each other through relatively weak interlayer O−H···O hydrogen bonds into the final frameworks. This microscopic blue script suggests that the final assemblies of Ag(I)/DL-Cys should be 2D achiral sheets.

The above deduction was justified by an experiment in which 2D nanosheets with a typical thickness of ∼800 nm were obtained under the same reaction conditions except that DL-Cys rather than homochiral Cys was chosen to assemble with Ag(I) (Figure 8). UV−vis characterization showed the same shoulder peak at ∼370 nm as in the helical nanobelts. However, the CD spectrum of the nanosheets showed no chiral peaks, meaning that the Ag(I)/DL-Cys nanosheets were achiral and that L-Cys and D-Cys were kept in a molar ratio of exactly 1:1 in the sheets. Changing the ligand's chirality from homochiral to racemic greatly influenced not only the chirality (from homochiral to achiral) but also the dimensionality (from 1D to 2D) of the final self-assembled Ag(I)/Cys BCP products.

Conclusions

In summary, chirality transcription from molecules to frameworks in Ag(I)/Cys BCPs has been elucidated by both experimental and computational studies. This is significant for understanding many biorelated self-assembly processes spanning from the molecular scale to the macroscale. Coupling the chirality of amino acid molecules into coordination frameworks allows the structure, morphology, and electro-optical properties of the MOF assemblies to be tailored on purpose. This shall enrich our toolbox for constructing chirality-regulated functional materials with potential applications in nanoelectronics and nanophotonics.[24]

Acknowledgment. We thank the National High-Tech Research and Development Program (2007AA03Z302 to Z.T.), the 100-Talent Program of the Chinese Academy of Sciences (Z.T.), the National Science Foundation of China (20973047 to Z.T. and 20933008 to K.D.), the National Research Fund for Fundamental Key Project (2009CB930401 to Z.T.), and the Knowledge Innovation Program of the Chinese Academy of Sciences (KJCX2-YW-M04 to K.D.) for financial support of this research.

Supporting Information Available: Detailed materials and methods, additional experimental data, and details of DFT simulations. This material is available free of charge via the Internet at http://pubs.acs.org.

JA102827F

(24) (a) Xia, Y. N.; Yang, P. D.; Sun, Y. G.; Wu, Y. Y.; Mayers, B.; Gates, B.; Yin, Y. D.; Kim, F.; Yan, H. Q. *Adv. Mater.* **2003**, *15*, 353–389. (b) Wang, D. H.; Luo, H. M.; Kou, R.; Gil, M. P.; Xiao, S. G.; Golub, V. O.; Yang, Z. Z.; Brinker, C. J.; Lu, Y. F. *Angew. Chem., Int. Ed.* **2004**, *43*, 6169–6173. (c) Srivastava, S.; Santos, A.; Critchley, K.; Kim, K. S.; Podsiadlo, P.; Sun, K.; Lee, J.; Xu, C. L.; Lilly, G. D.; Glotzer, S. C.; Kotov, N. A. *Science* **2010**, *327*, 1355–1359.